ADVANCED MATERIALS

Supporting Information

Electron Beam Lithography of Magnetic Skyrmions

Yao Guang, Yong Peng, Zhengren Yan, Yizhou Liu, Junwei Zhang, Xue Zeng, Senfu Zhang, Shilei Zhang, David M. Burn, Nicolas Jaouen, Jinwu Wei, Hongjun Xu, Jiafeng Feng, Chi Fang, Gerritvan der Laan, Thorsten Hesjedal, Baoshan Cui, Xixiang Zhang,* Guoqiang Yu,* and Xiufeng Han

Electron beam lithography of magnetic skyrmions

Yao Guang†[1,2], Yong Peng†[3], Zhengren Yan†[1,2], Yizhou Liu[1,2], Junwei Zhang[3,4], Xue Zeng[5], Senfu Zhang[4], Shilei Zhang[6,7], David M. Burn[8], Nicolas Jaouen[9], Jinwu Wei[1,2,10], Hongjun Xu[1,2,10], Jiafeng Feng[1,2], Chi Fang[1,2], Gerrit van der Laan[8], Thorsten Hesjedal[11], Baoshan Cui[10], Xixiang Zhang[4]*, Guoqiang Yu[1,2,10]*, Xiufeng Han[1,2,10]

[1]Beijing National Laboratory for Condensed Matter Physics, Institute of Physics, Chinese Academy of Sciences, Beijing 100190, China

[2]Center of Materials Science and Optoelectronics Engineering, University of Chinese Academy of Sciences, Beijing 100049, China

[3]Key Laboratory for Magnetism and Magnetic Materials of Ministry of Education, Lanzhou University, Lanzhou 730000, China

[4]Physical Science and Engineering Division (PSE), King Abdullah University of Science and Technology (KAUST), Thuwal 23955-6900, Saudi Arabia

[5]School of Mathematics and Physics, Lanzhou Jiaotong University, Lanzhou, 730070, China

[6]ShanghaiTech Laboratory for Topological Physics, ShanghaiTech University, Shanghai 201210, China

[7]School of Physical Science and Technology, ShanghaiTech University, Shanghai 201210, China

[8]Diamond Light Source, Harwell Science and Innovation Campus, Didcot, Oxfordshire, OX11 0DE, UK

[9]Synchrotron SOLEIL, L'Orme des Merisiers, Saint-Aubin, 91192 Gif-sur-Yvette, France

[10]Songshan Lake Materials Laboratory, Dongguan, Guangdong 523808, China

†These authors contributed equally to this work.

[11]Department of Physics, Clarendon Laboratory, University of Oxford, Oxford OX1 3PU, UK

Email address: guoqiangyu@iphy.ac.cn, xixiang.zhang@kaust.edu.sa

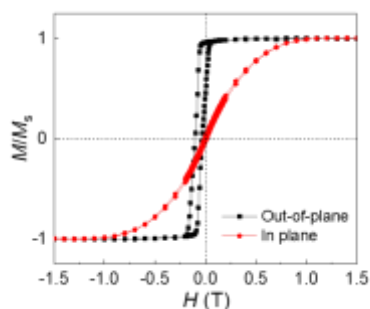**S1. Magnetic hysteresis loops and zero-field magnetic domain structure**

Figure S1. Out-of-plane and in-plane hysteresis loops for the annealed sample. The out-of-plane hysteresis loop is from the Fig. 1c in the main text.
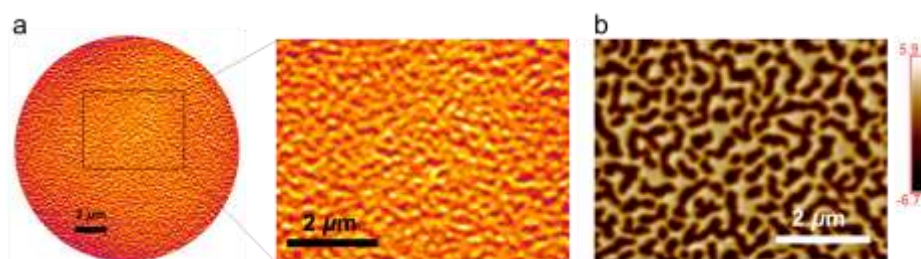

Figure S2. (a) Zoomed-in area (black square) in the Lorentz transmission electron microscopy (LTEM) image shown in Fig. 1d. (b) Magnetic force microscopy (MFM) image of the magnetic domains at zero-field and room temperature on an as-grown sample. The scale bars are 2 μm.

Figure S2a shows the zoomed-in area in the Lorentz transmission electron microscopy (LTEM) image in Fig. 1d in the main text. The bright and dark contrast can be clearly observed in the image, which has been well explained by the Lorentz force-induced electron deflection due to in-plane magnetic fields. The bright or dark contrast corresponds to the boundary between two adjacent perpendicularly magnetized magnetic domains. The characteristic domain size estimated from LTEM at zero field

is comparable to that observed in magnetic force microscopy (MFM), as shown in Figure S2b.

S2. Lorentz transmission electron microscopy images of a Ta(2 nm)/[Pt(3 nm)/Co(2 nm)/Ta(2 nm)]$_{10}$ multilayer.
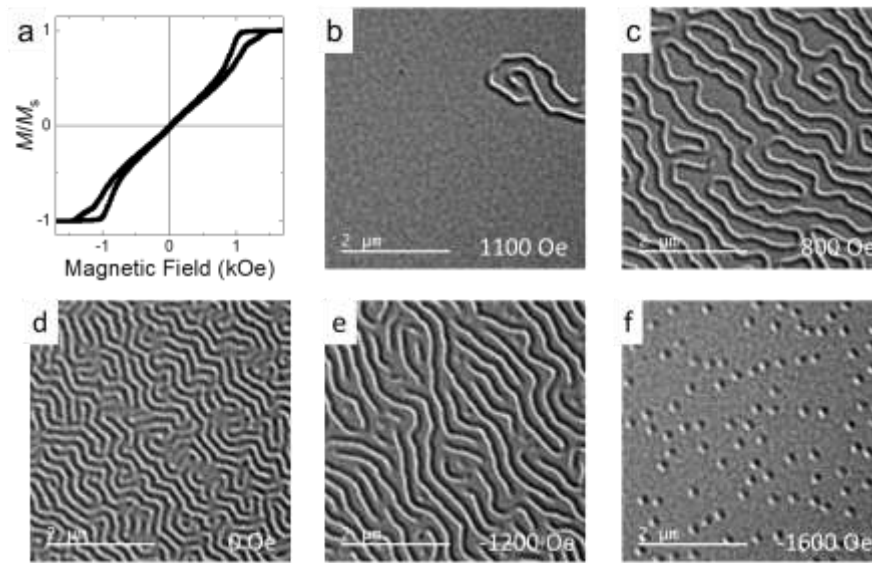

Figure S3. (a) Normalized out-of-plane magnetic hysteresis loop of a Ta(2 nm)/[Pt(3 nm)/Co(2 nm)/Ta(2 nm)]$_{10}$ multilayer sample, measured at room temperature. (b)–(f) In-situ room-temperature LTEM images captured at different magnetic fields for the magnetic field decreasing from positive saturation to negative saturation field.

Figure S3a shows the normalized out-of-plane magnetic hysteresis loop of a Ta(2 nm)/[Pt(3 nm)/Co(2 nm)/Ta(2 nm)]$_{10}$ multilayer sample, which was measured at room temperature. At zero field, the remanent magnetization is almost zero since there is no exchange bias in this structure. Figures S3b-f show the LTEM images under

different magnetic fields. When the magnetic field is decreased from the positive saturation field to 1100 Oe (Fig. S3b), snake-like stripe domains emerge from the ferromagnetic state. As the field is further decreased to 800 Oe, the snake-like domains become longer (Fig. S3c). At zero magnetic field, a labyrinthine domain structure is formed (Fig. S3d). As the field is increased in the opposite direction (negative field), this labyrinth domain structure gradually breaks up into smaller pieces, and a mixed state of skyrmions and snake-like domains emerges (Fig. S3e). Subsequently, more and more skyrmions form and the skyrmion density reaches its maximum when the field reaches -1600 Oe (Fig. S3f).

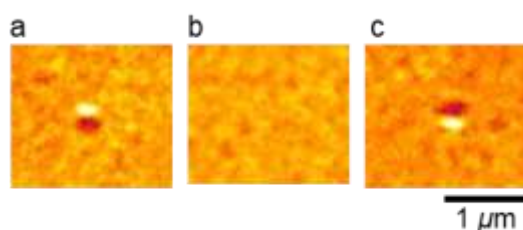## S3. Lorentz transmission electron microscopy images of a single skyrmion

Figure S4. LTEM images of a skyrmion at a tilt angle of (a) 28.2º, (b) 0º, and (c) -28.2º. No contrast is observed for a tilt angle of 0º. The scale bar is 1 μm.

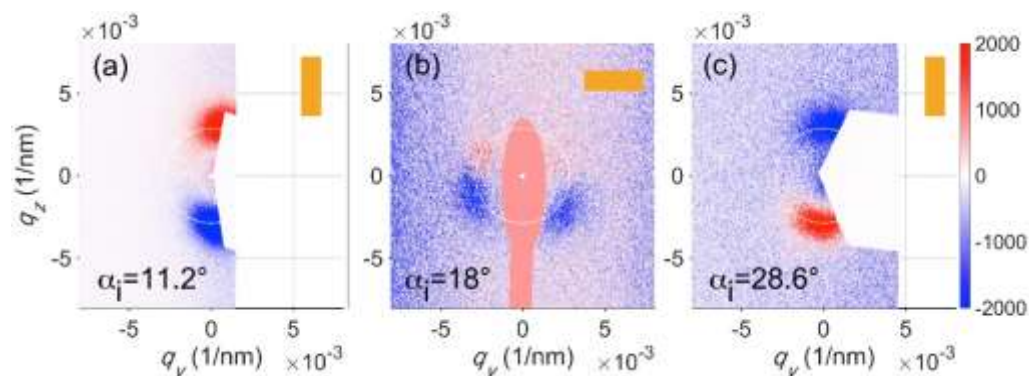## S4. Demonstration of a depth-dependent chirality of the domain walls

Figure S5. Circular dichroism (CD) resonant elastic x-ray scattering (REXS) results. (a) CD-REXS pattern at an incidence angle of 11.2°. The sample has a rectangular shape, and it is oriented as indicated by the top-right yellow rectangle. The domain wall propagation wavevector is along the long edge. (b) After rotating the sample by 90°, the extinction line, separating positive and negative contrast, is well observed. (c) CD-REXS pattern at a larger incidence angle of 28.6°. The sample rotation is the same as in (a), indicated by the yellow rectangle shown in the inset.

Circular dichroic resonant elastic x-ray scattering (CD-REXS) experiments were carried out on the same sample at the Sextants beamline at the synchrotron SOLEIL, as well as at beamline I10 in Diamond Light Source, in order to determine the exact ground-state magnetic structure. CD-REXS has been successfully applied in our previous studies on chiral magnetic materials, demonstrating its powerful capability for revealing the periodicity of the magnetic domains, the domain wall type (i.e., being Néel-type or Bloch-type, or anywhere inbetween), as well as the depth-dependent profile of the magnetization twist (*1-4*). The direct result from CD-REXS is the reciprocal space dichroism pattern in the q_x-q_y plane, obtained by the

scattering intensity difference of left- and right-circularly polarized light, using a photon energy matching the absorption edge of the magnetic element. If the real-space magnetic domain wall propagates along a certain direction, a pair of magnetic peaks is observed. On the other hand, if the magnetic domain walls are not locked along a specific orientation (such as for maze domains), a ring-like magnetic scattering pattern occurs. In both scenarios, dichroic patterns, i.e., half-positive-half-negative magnetic scattering signals will appear. More importantly, a dividing line that passes through the reciprocal space center, called *dichroism extinction line*, can be defined. The azimuthal angle of such an extinction line unambiguously reveals the domain wall type, i.e., a Néel-type domain wall leads to a horizontal extinction line, while a Bloch-type wall gives rise to a vertical one.

We performed CD-REXS on the sample under zero magnetic field, and in a temperature range from 300-420 K, although no obvious temperature dependence is observed. Figure S5a shows the CD-REXS pattern at the Co L_3 edge (777.6 eV) with an incidence angle of 11.2°. At this angle, the soft x-rays only probe the top few nanometers of the sample. The Friedel pair of the magnetic peaks reveals a domain wall periodicity of 350 nm. The color configuration, i.e., top-red-bottom-blue coding, excludes the possibility of a Bloch-type domain, whose dichroism otherwise would be smeared out due to the extinction effect. By rotating the sample by 90°, as shown in Fig. S5b, a well-defined extinction line can be observed. Its horizontal direction indicates the Néel-type character of the domain wall from the very top surface. Moreover, by increasing the incidence angle, the probing depth increases, such that

soft x-rays are more sensitive to the entire stack of the multilayer. As shown in Fig. S5c, the dichroism reversal phenomenon can be observed (top-blue-bottom-red coding), suggesting the chirality flip of the Néel domain wall at the bottom layer. Such a three-dimensional domain wall structure, with opposite chiral Néel-type domain walls on the two surfaces, was elaborated in previous work (*4*).

S5. Electron-beam-induced thermal effect

Many experiments have reported the heating effect induced by electron beam exposure (*5-9*). The electron-beam-induced temperature increase can be described by (*8*):

$$T = T_{R_0} + \frac{1}{4k}JR_0^2 - \frac{1}{4k}Jr^2$$

$$J = \frac{Q}{\pi R_0^2} = J_e \cdot \left(\frac{dE}{dx}\right) \cdot h$$

$$T_{R_0} = T_{RT} + \frac{1}{4k}JR_s^2 + \frac{Q}{2\pi kh}ln\frac{R_s}{R_0}$$

$$T(r = 0) = T_{RT} + J_e[\frac{1}{4k}\left(\frac{dE}{dx}\right)hR_s^2 + \frac{\left(\frac{dE}{dx}\right)R_0^2}{2k}ln\frac{R_s}{R_0} + \frac{1}{4k}\left(\frac{dE}{dx}\right)hR_0^2]$$

where T is the temperature at the center of the illumincated area, T_{R_0} is the temperature at the edge of the illuminated area (with an area of πR_0^2), k is the thermal conductivity, J is the density of heat flux, r is the distance to the center of the heat source, Q is the total heat input, h is the film thickness, J_e is the electron current density, E is mean energy of the incident electron, and dE/dx is the energy loss per electron, R_s is the distance from the heat sink to the irradiated area, and T_{RT} is room temperature.

The temperature profile around the illumination area can thus be calculated and a

key parameter for the temperature increase is the electron current density J_e. For the illumination case shown in Fig. 1, using the following physical parameters: $k = 200$ W/m·K, $J_e = 2.7$ e nm^{-2} S^{-1}, $h = 6$ nm, dE/d$x = 80 \times 10^{-19}$ J/nm, $R_0 = 5500$ nm, $R_s = 100$ μm, and $T_{RT} = 300$ K, the calculated temperature profile is shown in Fig. S6. The central temperature can only rise to about 300.01 K. However, for the case of skyrmion creation, it is difficult to obtain the electron current density, so we cannot qualitatively obtain the increased temperature.

In the micromagnetic simulations, we found that the non-linear temperature profile can be simplified to a linear-type profile as shown in Fig. 2f without affecting the final results. Therefore, to optimize the simulation efficiency, a linear temperature profile is employed in the simulations.
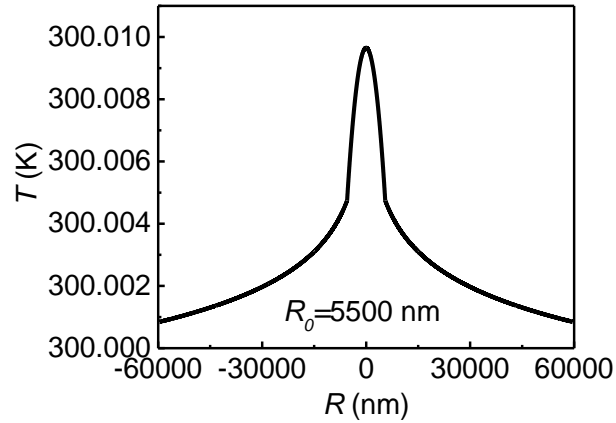

Figure S6. Heating effect induced by the electron beam with a radiation radius of 5500 nm.

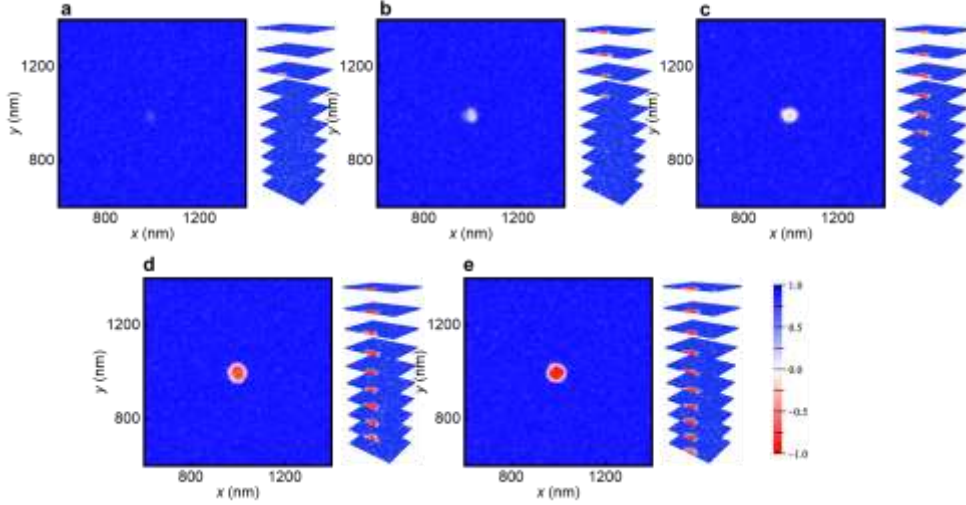## S6. Intermediate state during skyrmion creation

Figure S7. Simulated electron-beam-induced single skyrmion creation process. The skyrmion size is around 100 nm. (a)-(e), Snapshots of the single skyrmion creation process in the *x-y* plane at different time (t = 90, 160, 166, 175, and 180 ns). The color represents the averaged m_z across all the magnetic layers. The insets present the details of m_z for each layer from a sideview. The electron beam is applied within the circular region with 100 nm at t = 0 ns.

Using micromagnetic simulations, we reveal the intermediate states during the skyrmion creation. A magnetic multilayer with ten repetitions was simulated. The geometry of each magnetic layer is 2 μm × 2 μm × 0.6 nm with a mesh size of 8 nm × 8 nm × 0.6 nm. Different magnetic layers are separated by a 6.6 nm spacer. The following parameters were used in the simulations: exchange constant A = 10 pJ/m, DMI constant D = 1.35 mJ/m^2, PMA constant K_u = 965 kJ/m^3, saturation magnetization M_S = 1150 kA/m, and Gilbert damping constant α = 0.2. An out-of-plane external field, B_{ext} = 68.7 mT, is applied to simulate the exchange bias

effect of $Ir_{22}Mn_{78}$. A circular region with a radius of 50 nm is assumed to be illuminated by the electron beam. The simulations outside the circle were carried out at 300 K with an open boundary condition, while a linear temperature gradient is applied inside the circle with a center temperature of 400 K. The simulation results are shown in Fig. S7. The electron beam is applied at $t = 0$ ns. At $t = 90$ ns, the first skyrmion is created in the third layer as shown in the three-dimensional layer-resolved magnetic structure in Fig. S7a. As time passes, the skyrmion is gradually created in different layers. At $t = 180$ ns (Fig. S7e), skyrmions are created in all layers and become stable. For the intermediate states, the contrast of the center area (a, b, or c) is weaker compared to that of the final state (e).

1.   S. L. Zhang, G. van der Laan, T. Hesjedal, Direct experimental determination of spiral spin structures via the dichroism extinction effect in resonant elastic soft x-ray scattering. *Phys. Rev. B* **96**, 094401 (2017).
2.   S. L. Zhang, G. van der Laan, W. W. Wang, A. A. Haghighirad, T. Hesjedal, Direct Observation of Twisted Surface skyrmions in Bulk Crystals. *Phys. Rev. Lett.* **120**, 227202 (2018).
3.   S. L. Zhang *et al.*, Reciprocal space tomography of 3D skyrmion lattice order in a chiral magnet. *Proc. Natl. Acad. Sci.* **115**, 6386-6391 (2018).
4.   W. Li *et al.*, Anatomy of Skyrmionic Textures in Magnetic Multilayers. *Adv. Mater.* **31**, e1807683 (2019).
5.   T. Yokota, M. Murayama, J. M. Howe, In situ transmission-electron-microscopy investigation of melting in submicron Al-Si alloy particles under electron-beam irradiation. *Phys. Rev. Lett.* **91**, 265504 (2003).
6.   R. F. Egerton, P. Li, M. Malac, Radiation damage in the TEM and SEM. *Micron* **35**, 399-409 (2004).
7.   A. Reguer *et al.*, Probing the local temperature by in situ electron microscopy on a heated Si_3N_4 membrane. *Ultramicroscopy* **110**, 61-66 (2009).
8.   H. M. Zheng *et al.*, Observation of Transient Structural-Transformation Dynamics in a Cu_2S Nanorod. *Science* **333**, 206-209 (2011).
9.   J. J. Li, Y. P. Li, Q. Li, Z. C. Wang, F. L. Deepak, Atomic-scale dynamic observation reveals temperature-dependent multistep nucleation pathways in crystallization. *Nanoscale Horiz.* **4**, 1302-1309 (2019).